Taylor & Francis
Taylor & Francis Group

Experimental Investigation of Inertial Mixing in Colliding Droplets

BRIAN CARROLL and **CARLOS HIDROVO**

Mechanical Engineering Department, The University of Texas at Austin, Austin, Texas, USA

Achieving the increasingly fast mixing requirements posed by the chemical, biological, and life science community for confined microchannel droplet flows remains an engineering challenge. The viscous and surface tension forces that often dominate microflows undermine fast, efficient mixing. A novel mixing arrangement based on droplet collisions has been developed that significantly improves mixing rates by utilizing inertia to rapidly rearrange fluid contents. This article experimentally investigates inertial droplet mixing in micro-flows following high-speed droplet pair collisions. The technique utilizes a gaseous flow for liquid droplet generation and transport with collisions occurring in Y-junction microchannel geometries. Mixing rates are quantified using differential fluorescent optical diagnostics, custom image processing algorithms, and statistical analysis. Measured droplet mixing times are compared to the characteristic time scales for mass and viscous diffusion and bulk convective transport. Results show that mixing times are decreased as the droplet pair collision inertia is increased, indicating the potential benefit for inertial collision mixing.

INTRODUCTION

The turbulent flow regime easily exploited at the macroscale to increase mixing rates and sample homogenization is difficult and impractical to achieve in microfluidic devices due to conflicting length scales, dominance of surface forces, and the resulting low Reynolds (Re) number that characterizes conventional micro-flows. The success of the next generation of lab-on-a-chip (LOC) and micro total analysis systems (μTAS) is dependent upon achieving fast mixing rates using practical and highly adaptable techniques. Investigating chemical reaction mechanisms requires achieving molecularly mixed conditions significantly faster than the reaction kinetics under study. Proteomics is another emerging application for microfluidics that also requires substantial improvement in fluid mixing rates to accurately examine and statistically characterize folding kinetics. For example, a simple protein with 100 amino acids can fold 3^{198} different ways and sorts through these possibilities in a millisecond or less [1]. The ability to observe, characterize, and understand this critical process demands significant strides over

existing mixing techniques. As such, there is currently a push from these industries to achieve mixing rates that are on the order of microseconds for sample volumes in the nanoliter range.

All mixing, at the microscale or otherwise, is a diffusion-driven process once the molecular length scale is reached. It is the role of an effective micromixer to quickly and controllably rearrange the bulk fluid volume so that the diffusion process proceeds across the shortest length scale possible. In this sense, all mixing efforts are the same. The difference lies in how this length scale reduction is accomplished. Catalogued mixing methods are numerous and far reaching, spanning the spectrum from inherently complex to intuitively simple. An obvious delineation can be made between active and passive techniques. Active techniques include any methods that rely on means external to the device. These external perturbations can include acoustic [2–4], electrical [5–7], magnetic [8], thermal [9, 10], or mechanical [11]. Although these methods have been successful for specific applications, their use as a general mixing technique is limited since many microfluidic platforms are incapable of providing the required fluid properties and/or supporting architecture.

The two most prevalent and widely successful passive mixing techniques are hydrodynamic flow focusing and chaotic advection. Hydrodynamic flow focusing physically reduces the mixing length scale through geometric confinement. Although most hydrodynamic flow focusing devices use flow fields that are primarily laminar, turbulent flow regimes have been

successfully demonstrated [12]. The governing physics of laminar flow focusing are well understood and can be modeled using a fluid resistance network [13]. Mixing times near 1 μs have been achieved for focused widths near 50 nm [14, 15]. However, the flow focusing technique is only applicable to continuous flow systems.

Chaotic advection is a termed first coined by Aref in his seminal paper [16]. The publication of this paper in 1984 unknowingly spawned a new strategy for microscale mixing a decade later, and the term is now common within the microfluidic community. Unlike hydrodynamic flow focusing, chaotic advection reduces the diffusion length scale by particle motions that, when viewed from a Lagrangian perspective, appear random and chaotic. Additionally, chaotic advection is achievable with both continuous flow [17, 18] and droplet-based flows [19–22]. For continuous-flow mixers, geometric obstacles and channel texturing are used to facilitate chaotic motions in the flow that would otherwise be laminar and orderly. Chaotic advection in segmented and droplet-based mixers is realized through a combination of channel geometry and localized interactions between the discrete and continuous phase and channel walls. These interactions produce rolling, stretching, and folding behaviors that continuously increase the miscible fluid's interface area, thereby reducing the length over which diffusion must occur. The process is analogous to the classic lid driven cavity problem where the flow field is perturbed by constant, periodic, or aperiodic forces occurring at interface boundaries. In fact, the lid driven cavity represents a simple and well-characterized system for understanding the otherwise complex flow field that results as droplets are transported inside microchannels [23]. Although mixing times near 1 ms have been achieved with chaotic advection [18], the majority of demonstrations remain in the 0.1–1 s range for picoliter fluid volumes [17, 20, 24, 25].

Given the wide range of mixing techniques currently employed, no one method completely satisfies all metrics required to meet the current demands of the next generation of μTAS and LOC devices. These metrics include high mixing rates, increased detection sensitivity for downstream components, high droplet throughput, fluid compatibility, and straightforward integration and implementation of system hardware. Because mixing time is proportional to the square of the characteristic length scale, reducing the length for mass diffusion significantly increases mixing rates, as indicated by hydrodynamic focusing efforts. A physical reduction in the system length scales, however, can result in detection-limited volumes and decreased throughput. Instead, the most effective micromixers reduce the length scale for diffusion by inducing flow patterns that continually stretch, fold, and swirl the scalar field (concentration, temperature, etc.). This process exponentially reduces the effective length over which mass diffusion must occur. The challenge is inducing these flow patterns quickly and controllably.

An alternative to existing mixing technologies that potentially satisfies the metrics just outlined is an inertial-based droplet micromixer, as shown in Figure 1. This system promotes mixing by utilizing the inertia of two approaching droplets. Each
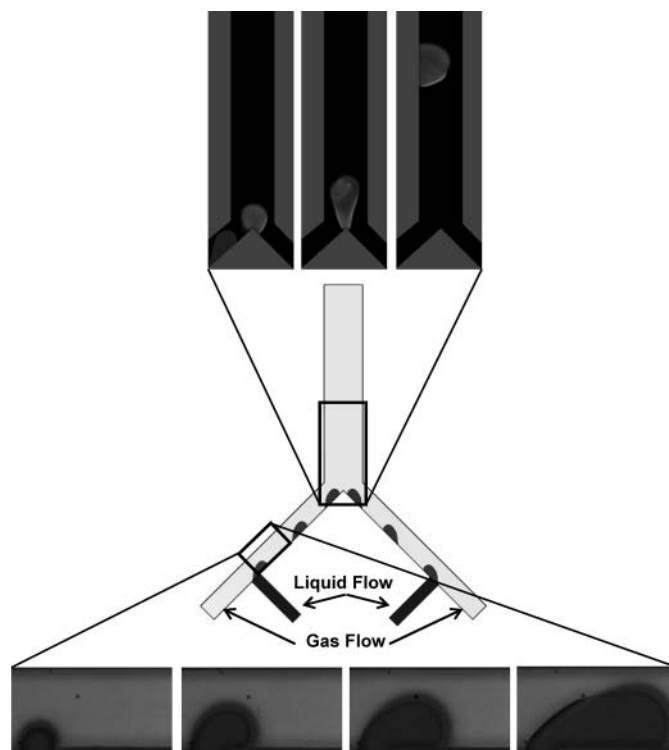

Figure 1 Solid model of an inertial micromixer using a Y-junction collision geometry and indicated inlets for liquid and gas flow. High speed images show the droplet growth and detachment at a T-junction (bottom) and droplet collision and mixing at a Y-junction (top).

droplet is delivered to a collision zone using a gaseous flow where *Re* in excess of 300 can be achieved with modest pressure drops (<10 psi). The gaseous flow detaches discrete liquid droplets from two opposing legs of a standard T-junction through a combination of inertial and hydrodynamic forces [26, 27]. Each droplet is delivered to a common junction and the opposing droplets collide under highly inertial conditions. The rapid droplet detachment rate ensures frequent droplet collisions. The coalesced and mixed solute volume is removed through a common exit channel.

Experimental results presented herein show that mixing times on the order of microseconds for liquid volumes in the nanoliter range are achievable using this technique. Mixing rates are increased because the direction of fluid advection and molecular diffusion are continually rearranged while the inertia is dissipated through viscous dissipation. This contrasts with parallel flow mixing schemes such as flow focusing. It is therefore anticipated that droplet mixing time should be inversely proportional to inertia and mass diffusivity while proportional to viscosity, such that:

$$t_{Mix} \sim \frac{Sc^{\alpha}}{Re^{\beta}} \tag{1}$$

In this relation, α and β are positive numbers and *Sc* is the Schmidt number (ratio of viscous to molecular diffusivity). Note that the ratio of *Re* and *Sc* number gives the Peclet (*Pe*) number, such that Eq. (1) can be written as a ratio of fluid properties and

Pe. For constant mass diffusivity and viscosity, the mixing time scale reduces to:

$$t_{Mix} \sim \nu^{\alpha+\beta} D^{\alpha-\beta} \frac{1}{Pe^{\beta}} \sim \frac{1}{Pe^{\beta}} \qquad (2)$$

Assuming a square dependence on *Pe* number, increasing the droplet relative velocity by a factor of two would decrease the mixing time by a factor of four for a convection dominated process.

The mixing rates are quantified using differential fluorescent measurements where opposing droplets are doped with different concentrations of a common fluorophore. The fluorophores absorb light at a particular preferred wavelength, are excited to a higher energy level, and quickly return to the ground state by emitting a lower energy and longer wavelength signal. The intensity of the emitted signal is related to the concentration of the fluorophore within the imaging volume. After proper spectral filtering, this signal is captured digitally at prescribed time intervals using a high-speed, CMOS camera. Custom image processing algorithms track the fluid volumes throughout the dynamic event. Quantitative mixing information is realized by executing a statistical analysis of the fluorophore spatial intensity distribution, where a uniform and homogeneous distribution indicates a well-mixed condition.

Once mixing times for a representative range of droplet *Re* numbers are presented, an order-of-magnitude analysis is conducted to understand the significance of the experimental results. Three different time scales are compared to the actual mixing time: molecular diffusion, viscous diffusion, and bulk convective transport. The analysis indicates that the mixing time, although always more, is of the same order as the convective transport time scale for the range of *Re* numbers considered. Compared to the time scales for molecular and viscous diffusion, mixing time is 10^6 and 10 times less, respectively. Scaling arguments also show that the ratio of the effective diffusion length to the droplet length scale is proportional to $Pe^{-1/2}$.

DEVICE DESIGN AND FABRICATION

Different collision zone geometries were designed, fabricated, and characterized. The collision arrangements examined included a standard head-on T-junction, a modified reduced area T-junction (nozzle), and a Y-junction channel geometry. Substantial testing of each design revealed that the Y-junction geometry promoted increased collision rates and facilitated mixed solute removal from the collision zone. The T-junction suffered from a droplet dead zone that prohibited the continuous phase from entirely removing the newly coalesced droplet. This dead zone also contributed to reduced droplet velocity just prior to collision. Conversely, the nozzle geometry accelerated droplets prior to collision but also elongated droplets due to the reduced flow area. Thus, the results presented in this article focus only on the Y-junction collision geometry with representative dimensions shown in Figure 2.
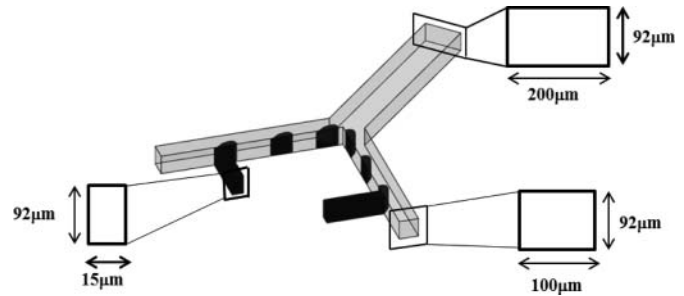

Figure 2 CAD image and pertinent dimensions of the Y-junction droplet collision device used to examine droplet mixing behavior.

The mixing device is fabricated using soft lithography techniques and polydimethylsiloxane (PDMS). The process flow shown in Figure 3 depicts the major fabrication steps. The microfabrication process involves creating a negative mold of the microchannel geometry on a standard 4-inch-diameter, 500-μm-thick silicon substrate. The wafer is cleaned and prepared using standard procedures. A negative near-ultraviolet (near-UV) resist (SU8-2050 MicroChem Corp.) is spin coated onto the wafer to a thickness dictated by the microchannel depth. The coated wafer is then baked to remove the solvents in the resist. Once cured, the wafer is placed in a Karl Suss MA6 mask aligner and exposed to 392-nm radiation through a mask containing the microchannel image. Since the smallest feature size on the microchannel is typically 20 μm, a photo-plotted, 7-mil film mask is used as an alternative to a chromium mask. The exposed wafer is then developed using the appropriate developer solution and baked at the prescribed temperature and duration.

Once the negative microchannel mold is complete, the PDMS solution is prepared. Sylgard 184 silicone elastomer base is mixed with a curing agent at a 10:1 weight ratio. The resist-coated wafer is treated with trichlorosilane to render the surface hydrophobic prior to pouring the PDMS. Once the PDMS solution is poured onto the silicon mold, the assembly is placed in a vacuum desiccator to promote solvent vaporization and air bubble removal. The assembly is then placed on a hot plate in ambient surroundings and baked at 45°C for approximately 3–6 h. The PDMS is peeled from the silicon substrate following the baking process and each device is cut in a rectangular shape and prepared for fluid and gas porting. A 2-mm-diameter belt-hole puncher is used to core the PDMS device at each gas and
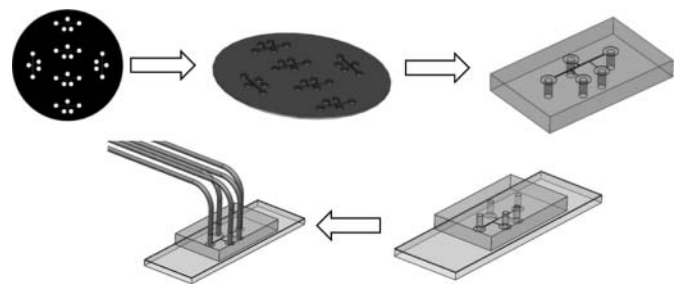

Figure 3 Process flow for PDMS soft lithography: mask CAD design, photolithography, molding, bonding, and fluid and gas tubing integration.

fluid inlet. A 1×3-inch standard microscope slide spin coated with a layer of PDMS $\sim 5\,\mu m$ thick provides a rigid substrate for bonding and ensures light transmission for inverted microscope visualization. Bonding is performed using a Harrick plasma cleaning machine. An ionized oxygen flow interacts with the PDMS and briefly renders the surface hydrophilic. Each device is then bonded to the slide and baked at $65°C$ for 4 h to improve bond strength. The finished device is then checked for dimensional integrity using a microscope and checked for leaks using a pressure source and flow meter.

EXPERIMENTAL SETUP

Observation and measurement of droplet mixing in a confined microchannel requires a robust and highly adaptable experimental setup. A custom microfluidic test bed has been designed and developed for experimental investigation of multiphase flows, particularly gas–liquid droplet flows. The test bed consists of a host of pressure transducers (Validyne P855 digital differential pressure transmitter) and mass flow sensors (Sierra Smart-Trak2) for real-time data acquisition. Gas and liquid flow control is realized using current-source pressure regulators (Proportion-Air QPV1) for gas flows and a constant displacement syringe pump (Harvard Apparatus PHD2000) for liquid flows. Visualization and image acquisition is facilitated by an inverted, reflected light microscope (Nikon Ti-U) and high-speed CMOS digital cameras. The cameras are each 12-bit monochrome and have a maximum resolution of 1024×1024 at $20\,\mu m$/pixel (Photron SA5) and 800×600 at $22\,\mu m$/pixel (Vision Research Phantom V7.1). Maximum frame rate is 1.3 MHz (Photron SA5) and 0.17 MHz (Vision Research Phantom V7.1). All instruments and acquisition equipment are routed through a dedicated host computer. A LabView Virtual Instrument (VI) has been developed to provide real time user control and system diagnostics of all instrumentation except for the cameras, which use vendor-specific software. A schematic and actual image of the experimental setup is shown in Figure 4.

The microscope is fitted with an epifluoresence optical assembly that includes beamsplitters and filters. The optical specifications are determined by the particular fluorophore selected. Pyrromethene 556 is used as the tracer dye for these tests and has maximum absorption near 500 nm (blue) and maximum fluorescence near 535 nm (green), providing a Stokes shift of 35 nm. The adsorption and emission spectrum of Pyrromethene 556 in distilled water is shown in Figure 5. Figure 6 illustrates the optical path of excitation and emission light. A 200-W metal halide white light (Prior Scientific Lumen 200) is used for fluorophore excitation. A cleanup filter transmits only blue wavelengths from the white light source. The beamsplitter reflects the blue wavelengths onto the back aperture of the microscope objective. The $20\times$ Plan Fluor objective, with a numerical aperture of 0.45, illuminates the sample volume and excites the fluorophore. Fluorescent emission from the dye passes back through the objective and beam splitter and the signal is cleaned
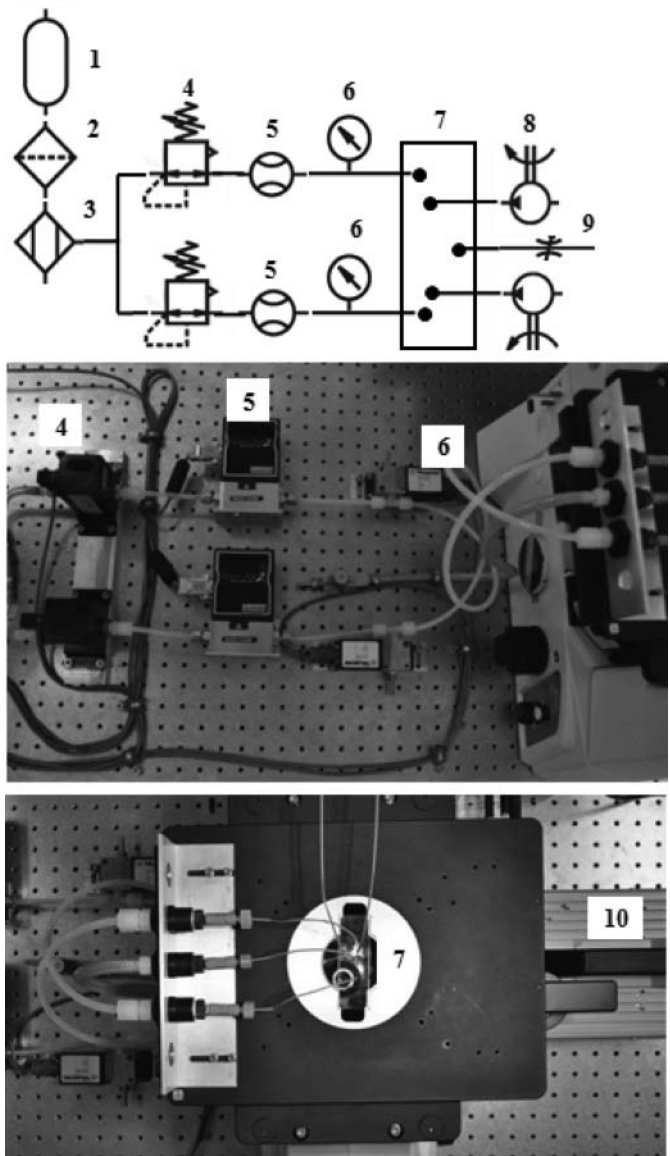

Figure 4 Simple schematic and actual images of experimental setup used for testing droplet mixing. The numbered devices are: high pressure gas source (1), micron filter (2), dryer (3), pressure regulators (4), mass flow meters (5), pressure transducers (6), microfluidic sample (7), syringe pump (8), needle valve (9), and high speed CMOS camera (10).

up using a narrow-pass green filter. The beam splitter ensures that any reflected excitation light is removed and the narrow pass filter removes any light with wavelengths greater than the maximum fluorophore emission. Thus, only light within the wavelength range 500–550 nm is captured by the camera.

OPTICAL DIAGNOSTICS

Quantifying mixing in microfluidic device requires different techniques from those used at the macroscale. The small volumes in consideration (10–100 nl) and relatively fast time scales (10 μs) make optical diagnostics the obvious choice.
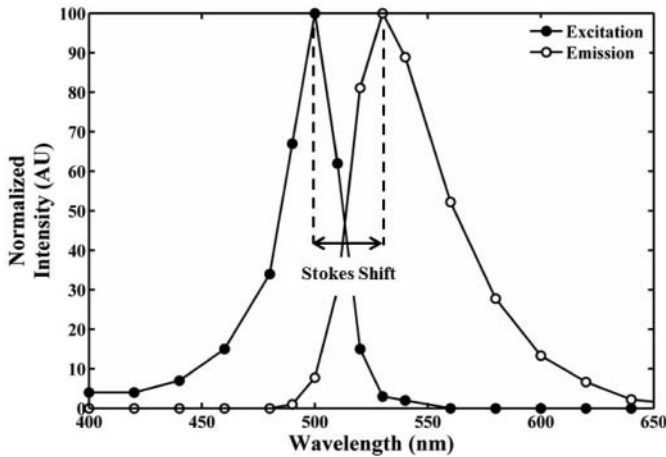
Figure 5 Adsorption and emission spectrum for Pyrromethene 556 in distilled water.

Within the optical diagnostic toolbox, three major techniques have been successfully demonstrated for mixing quantification: infrared absorption (IR), spontaneous Raman scattering (SRS), and laser-induced fluorescence (LIF). IR techniques measure the wavelength and intensity of mid-infrared (2.5–50 μm) light absorbed by a sample. Energy provided by the light source excites molecular vibrations to higher energy levels resulting in absorption bands that are characteristic of specific types of chemical bonds. SRS is an inelastic radiative scattering process that operates on the short lived "virtual" states and subsequent Raman shift. Both IR and SRS provide molecular fingerprints of chemical species present in the investigation region such that the local concentration, and hence degree of mixing, are resolved. LIF is also an inelastic radiative process but is based on

the absorption and subsequent emission of a photon following quantum energy state interactions. By controlling environmental parameters, such as temperature and pH, and ensuring optically thin conditions, the spatial distribution of the received LIF emission signal can be used to determine the degree of sample homogenization.

The LIF application presented herein is the time resolved microscopy visualization and quantification of the spatial concentration distribution of a fluorescing tracer dye following high-speed droplet collisions. The focus is on passive mixing, where the flow is unaffected by the scalar field yielding Level 1 type mixing [28]. A single fluorophore dye is used and the interrogation volume remains at a uniform temperature and pH throughout the mixing event. Mixing information is provided by the statistics of the captured fluorescent intensity field, where the driving statistic is the standard deviation:

$$\sigma_f = \left[\frac{\sum_{i=1}^{N}(I_{f,i} - \mu_f)^2}{N_f} \right]^{\frac{1}{2}} \tag{3}$$

In this relation, σ_f, μ_f, and N_f are the intensity standard deviation, average intensity, and number of participating pixels for frame f. It is important to note that only pixels located within the droplet volume for each image frame are used for statistical analysis. Because the standard deviation is sensitive to the absolute magnitude of the intensity field, it is necessary to normalize this statistic by the mean intensity value. This allows direct comparison of statistics from different experiments where the excitation illumination strength may have differed. For instance, if the intensity of the white light source is doubled while the fluorophore concentration remains unchanged, the standard deviation would yield a different result even though the concentration field remains unchanged. Normalizing all participating pixels by the average frame intensity resolves this issue:

$$\frac{\sigma_f}{\mu_f} = \left[\frac{\sum_{i=1}^{N}(\frac{I_{f,i}}{\mu_f} - 1)^2}{N_f} \right]^{\frac{1}{2}} \tag{4}$$

To illustrate this procedure, consider two droplets colliding at the apex of a Y-junction, as shown in Figure 7 (the Y-junction geometry is outlined in the first image frame). A droplet with high concentration (0.7 mg/mL) is perched at the apex and a second droplet of low Pyrromethene 556 concentration (0.07 mg/mL) approaches the collision zone from the lower right. The two droplets collide with a relative velocity in the 0.5 m/s range. Upon collision, the kinetic energy carried by each droplet is viscously dissipated through complex vortical motions. The coalescing droplet volume is quickly rearranged, providing an exponential increase in fluorophore interfacial area. This rapid decrease in mixing length accelerates the mixing process.

Each droplet volume prior to and during the mixing event is tracked using a custom image processing algorithm, and the volumetric fluorophore intensity field for each image frame is statistically evaluated. The plot shown in Figure 8 shows the time history of the intensity statistics (average intensity and
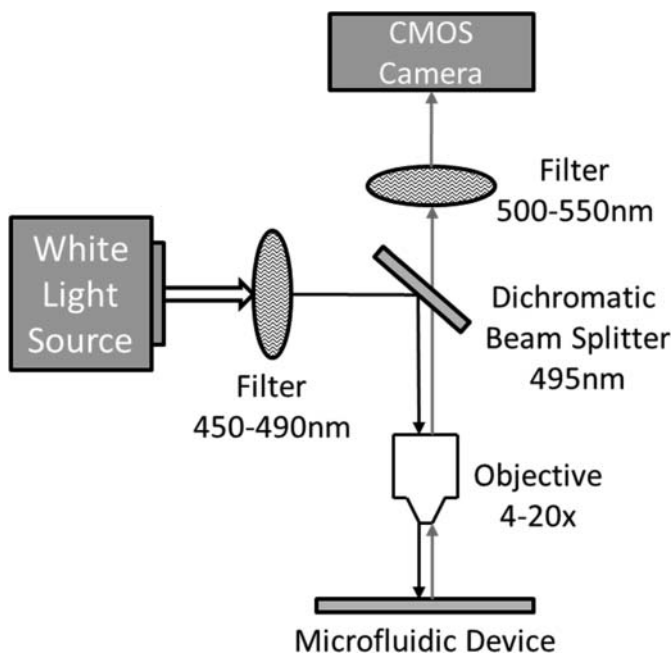

Figure 6 Schematic of optical assembly used for fluorescent measurements.
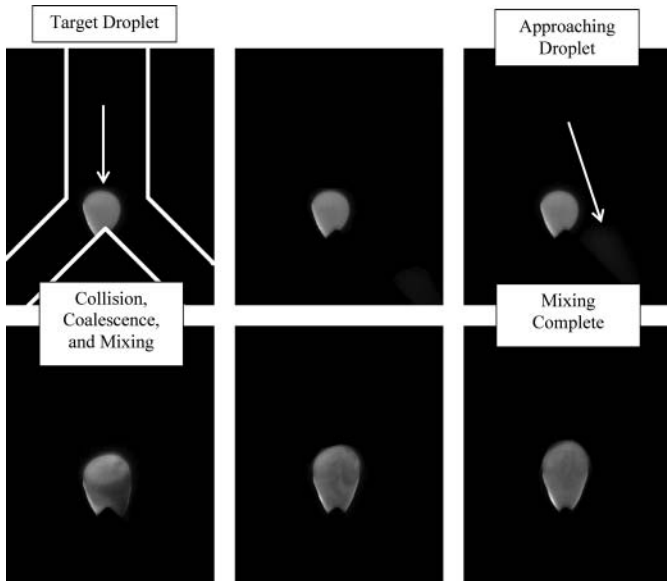
Figure 7 Series of high speed images taken at 10,000 fps showing a droplet collision and subsequent mixing event. Droplet intensity distribution is proportional to Pyrromethene 556 concentration. The image sequence corresponds to the mixing regions indicated on the statistical plot shown in Figure 8 as follows: single droplet perched on the apex of a Y-junction (0 ms), second droplet entering field of view from left (1.10 ms), both droplets in field of view just prior to collision (2.10 ms), mixing just after collision (2.70 ms), mixing continued (3.50 ms), and mixing complete (5.50 ms).

standard deviation) that correspond to the mixing event shown in Figure 7. The statistics clearly identify four distinct regions in the mixing process, as indicated by the dashed lines in Figure 8. Initially, the average intensity and standard deviation remain constant while only a single droplet is in view. As the second droplet enters the frame, the average intensity begins to decreases while the standard deviation increases. The spatial standard deviation reaches a maximum at the point of collision since there are two droplet volumes with significantly different intensities. As mixing progresses, the standard devia-
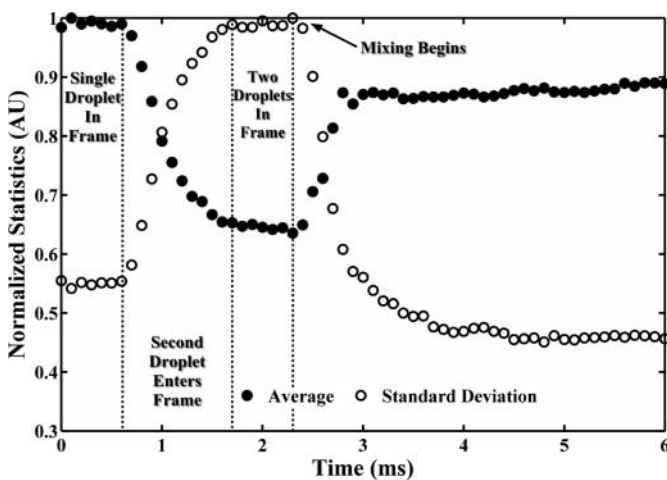

Figure 8 Statistical data for the droplet collision mixing event pictured in Figure 7 with identifiable regimes highlighted.
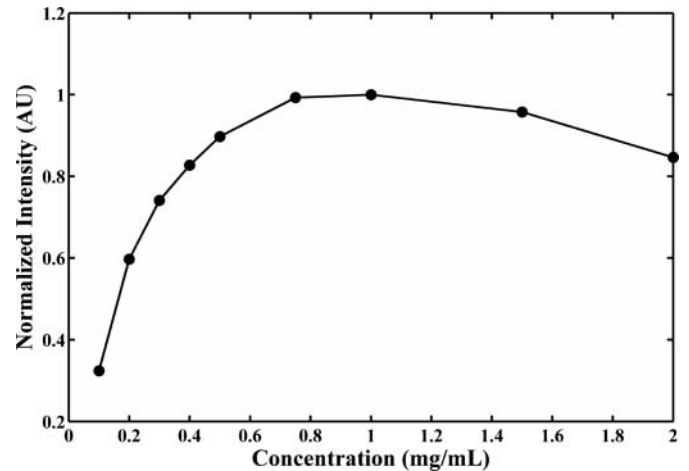

Figure 9 Pyrromethene 556 emission intensity for different fluorophore concentrations in distilled water. Data has been normalized by maximum intensity.

tion quickly decreases while the tracked droplet volume and average intensity remain unchanged. Mixing is assumed complete when the standard deviation reaches a minimum and is steady. Total droplet volume was calculated based on the number of pixels illuminated, the area of each pixel, and the depth of the channel.

It is important to note that the average intensity, based on the intensity distribution of both droplets, is not necessarily constant during the mixing event. The normalized average intensity of the combined droplet volumes ranges from 0.62 at collision (2.30 ms) to 0.9 when fully mixed (5 ms). This is due to the nonlinear variation of fluorescent intensity versus fluorophore concentration. Prior to the droplet mixing experiments, the fluorophore concentration was varied to understand how the emitted intensity changes. As shown in Figure 9, the emitted intensity is not monotonic with fluorophore concentration. There is a critical concentration for a given optical depth that provides maximum emission. At concentrations greater than the critical value, self-quenching begins to reduce the emitted intensity. In order to infer fluorophore concentration from emitted intensity, the maximum fluorophore concentration must be less than the critical concentration.

EXPERIMENTAL RESULTS

Because a high-speed gas flow is used to detach and transport droplets, it is necessary to know how the detached droplet geometry changes with the air Re number (based on the average gas flow velocity, channel hydraulic diameter, and gas viscosity). Experimental results showed that droplet height and length varied with $Re_{Dh}^{-1/4}$ for channel aspect ratios considered when non-dimensionalized by the channel hydraulic diameter [26]. This length scale reduction with increasing continuous phase velocity is a favorable trend for droplet mixing, where smaller droplets colliding at high velocities decreases the mass convection time scale. For purely diffusion-driven mixing, the

characteristic molecular diffusion time is proportional to the square of the characteristic diffusion length scale, L_{ch}, and inversely proportional to the mass diffusion coefficient, D. For Pyrromethene 556 in water, D is approximately 10^{-10} m^2/s [29]. This means that 1 min is needed to mix two 70-μm diameter droplets using diffusion alone. Mixing under inertial conditions, where the time for mass convection is much less than the time for mass diffusion, decreases the mixing time by orders of magnitude if implemented properly. To achieve mixing times on the microsecond scale, eight orders of magnitude reduction in total mixing time is required compared to a diffusion-driven mixing process.

To develop a link between mixing and droplet inertia, the Y-junction channel geometry depicted in Figure 2 was exercised and the optical diagnostic technique previously outlined was employed. The gas Re number was increased to produce smaller size droplets of increasing velocity. Image analyses of the frames just prior to collision were used to estimate droplet velocity and volume. This data provided the droplet Re number, defined as:

$$\text{Re}_{Droplet} = \frac{U_{rel} L_{ch}}{v_{Droplet}} \quad (5)$$

This droplet length scale is determined by the gas Reynolds number used to detach and entrain the droplets [26]. For the high-speed collisions presented herein, the droplet length scale ranged from 90 to 115 μm. The length scale for the collision process is based on the individual droplet length scales and is defined as:

$$L_{ch,Droplet} \equiv Vol_{Droplet}^{\frac{1}{3}} \quad (6)$$

The length scale for the collision process is then specified as:

$$L_{ch} \equiv \frac{2 L_{ch,Droplet1} L_{ch,Droplet2}}{L_{ch,Droplet1} + L_{ch,Droplet2}} \quad (7)$$

For two equal droplet volumes, the characteristic collision length scale is equal to the individual droplet length scale.

Experimental data of droplet mixing time versus droplet Re number is shown in Figure 10. The results show that mixing time
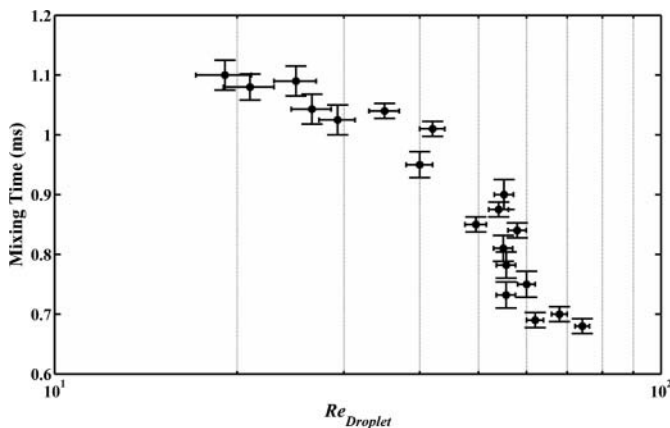

Figure 10 Graph of experimental results showing how droplet mixing time decreases with increasing droplet Reynolds number. Error bars indicate the uncertainty in the measurement process.

is reduced with increasing droplet inertia as initially proposed. The rate at which mixing time is reduced is not constant but increases with droplet Re number. This suggests an increasing contribution of droplet inertia prior to collision. The mixing time becomes proportional to $\text{Re}_{Droplet}^{-1}$ for $Re_{Droplet} > 30$. Error bars indicate the uncertainty in the measurement process. The source of these errors is the spatial resolution of the camera (1 μm at 20$\times$ and 2 μm at 10$\times$ magnification), temporal resolution of the camera (25–70 μs, depending on event), and device metrology measurements ($\pm$1 μm). The total error was determined using perturbation analysis.

RESULTS DISCUSSION

Because the focus of this work is inertial droplet mixing, it is fruitful to compare the measured droplet mixing times to other relevant time scales. These include time scales for molecular and viscous diffusion and bulk convection. The characteristic time for molecular diffusion is:

$$\tau_{Diff} \sim \frac{L_{ch,Diff}^2}{D} \quad (8)$$

This represents the time needed to diffuse mass one characteristic length in a fluid with mass diffusivity D. Similarly, the characteristic viscous diffusion time scale is:

$$\tau_{Visc} \sim \frac{L_{ch,Visc}^2}{v} \quad (9)$$

This scale represents the time required to diffuse momentum across some length scale in a fluid of kinematic viscosity v. Finally, the bulk convection time scale is:

$$\tau_{Conv} \sim \frac{L_{ch}}{U_{rel}} \quad (10)$$

The convective time scale can be viewed as the time required transporting material one droplet length scale at a rate equal to the relative droplet velocity. The length scale L_{ch} for mass and viscous diffusion and convection may differ. If the length scales are assumed equal and represented by the collision length scale, it is clear that the following must be true for inertial dominated mixing in large Schmidt number fluids:

$$\tau_{Diff} > \tau_{Visc} > \tau_{Conv} \quad (11)$$

It is not clear where the actual mixing time resides within these limits. The convective time scale tends to infinity as the velocity is reduced and approaches zero if velocity is increased indefinitely. The upper limit for mixing is dictated by the mass diffusion time scale and the lower limit by the convective time scale. The role of viscous diffusion is to dissipate inertia and determines how long the swirling, stretching, and folding motion is maintained. Since mixing is accelerated by such motion, the role of viscosity may place a limit on mixing rates. By taking the ratio of measured mixing time to the aforementioned characteristic time scales, insight is gained concerning inertial
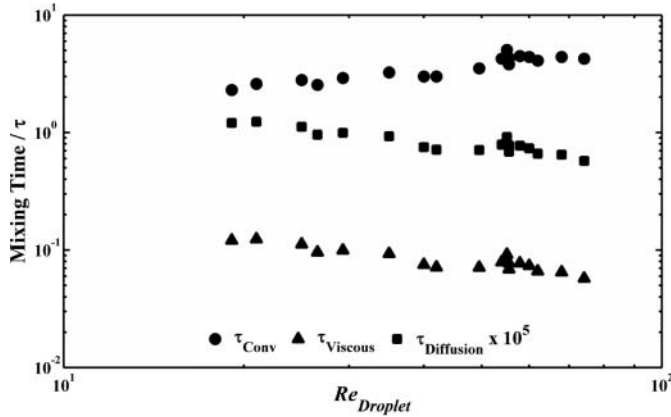
Figure 11 Graph showing the ratio of actual mixing time to mass diffusion, convection, and viscous diffusion versus droplet Reynolds number.

mixing. The plot in Figure 11 shows how each ratio changes with droplet *Re* number.

At the low droplet *Re* number range, the ratio of mixing time is on the order of that for convection, an order of magnitude less than that for viscous diffusion, and five orders of magnitude smaller than that for mass diffusion. As the droplet *Re* number increases, the ratio of mixing time to mass and viscous diffusion decreases while that for convection increases. The mixing to convection time ratio appears to reach a constant value past a droplet *Re* number of 30 and suggests that the ratio may become independent of droplet *Re* number as droplet inertia is increased.

Nondimensional numbers can be obtained directly from the characteristic time scales for mass diffusion, convection, and viscous diffusion. The ratio of viscous to convection time scales reduces to the droplet *Re* number:

$$\frac{\tau_{Visc}}{\tau_{Conv}} = \frac{L_{ch}^2/\nu}{L_{ch}/U} = \frac{U_{rel}L_{ch}}{\nu} = \text{Re}_{Droplet} \quad (12)$$

With this formalism, low *Re* numbers are dominated by the viscous diffusion time scales while high *Re* numbers are convective time scale driven. A *Re* number of unity implies that both time scales are of equal magnitude. For the droplet *Re* number considered in this work, it makes sense then that the droplet mixing time should be greater than that required for convection. Mixing cannot occur unless material is convected across the representative length scale. This rational is not valid, however, when the *Re* number is small since the convective time scale approaches infinity.

The ratio of the convective and mass diffusion time scales results in the *Pe* number:

$$\frac{\tau_{Diff}}{\tau_{Conv}} = \frac{L_{ch}^2/D}{L_{ch}/U} = \frac{U_{rel}L_{ch}}{D} = Pe_{Droplet} \quad (13)$$

In this context, the *Pe* number compares the relative magnitude of the mass diffusion and convective time scale. A high

Pe number indicates that the process is governed by convective effects and that mass diffusion is insignificant in the direction of bulk fluid motion. This is typically the case for fully developed duct flows. In the context of this work, the *Pe* number is on the order of 10^5 and suggests that the convection time scale dominates and, unlike laminar duct flow, bulk convective and diffusive motion are aligned. As shown in Figure 10, the mixing time to the convective time scale reaches a constant value once a *Re* number of 30 is exceeded. This suggests that the mixing time is directly proportional to the convective time scale:

$$t_{Mix} \sim \tau_{Conv} \sim \frac{L_{ch}}{U_{rel}} \quad (14)$$

This same result is found by scaling the convective-diffusive equation for a conserved scalar property.

The ratio of viscous to mass diffusion time scales gives the *Sc* number:

$$\frac{\tau_{Diff}}{\tau_{Visc}} = \frac{L_{ch}^2/D}{L_{ch}^2/\nu} = \frac{\nu}{D} = Sc \quad (15)$$

The *Sc* number compares the magnitude of the mass diffusion and viscous diffusion time scales. In a high *Sc* number process, momentum diffusion occurs much more rapidly than mass diffusion. The *Sc* number for this droplet mixing study is on the order of 10^4 and indicates that the viscous time scale is significantly less than that for mass diffusion.

All mixing regimes eventually become a mass diffusion process once the length scale is substantially reduced. This is the inherent benefit of flow focusing applications where flow patterning and geometric reductions increase mixing rates by reducing the length over which diffusion occurs. Using this formalism, an effective diffusion length scale for droplet collisions can be cast by equating the measured mixing time to the diffusion time scale. This can be viewed as the maximum possible length scale for mass diffusion in order to achieve the measured mixing time and is given by:

$$L_{eff,Diff} = \sqrt{t_{Mix}D} \quad (16)$$

Combining Eqs. (14) and (16) and rearranging results in a ratio of the effective diffusion length scale to the collision length scale that is inversely proportional to the *Pe* number:

$$\frac{L_{eff,Diff}}{L_{ch}} \sim Pe^{-\frac{1}{2}} \quad (17)$$

This simple result is analogous to laminar boundary layer flows in which the ratio of the boundary layer thickness (viscous diffusion length scale) to the body length scale (convective length scale) is proportional to $Re^{-1/2}$ (ratio of viscous and convective time scales). In the case of inertial droplet mixing, the appropriate nondimensional number is the *Pe* number (ratio mass diffusion and convective time scales).
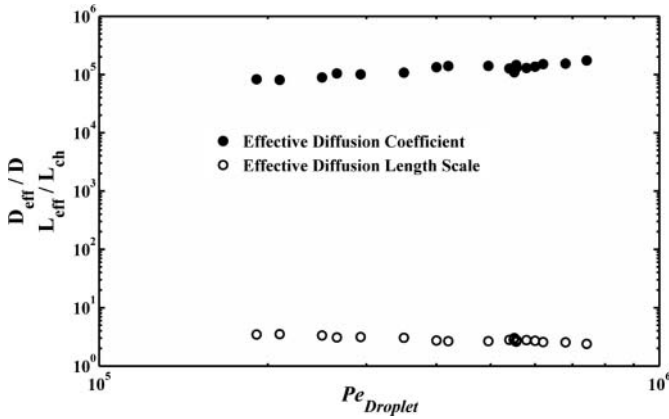
Figure 12 Graph of experimental data showing how the effective length and mass diffusivity ratio changes with droplet Peclet number.

In addition to defining an effective length scale for diffusion based on the measured mixing time, an effective diffusion coefficient can also be derived as:

$$D_{eff} \sim \frac{L_{ch}^2}{t_{mix}} \tag{18}$$

By combining Eqs. (14) and (18) and rearranging, a ratio of the effective and global mass diffusivity is produced that is proportional to Pe:

$$\frac{D_{eff}}{D} \sim Pe \tag{19}$$

The dependence of the effective length and mass diffusivity ratios on Pe number is shown in Figure 12. Note that as the Pe number increases, the effective diffusion length scale and effective diffusivity ratio have slopes of $-1/2$ and 1 on a logarithmic scale.

The increase in the effective mass diffusivity with Pe number verifies the assertion that droplet mixing rates increase with droplet inertia. However, droplet inertia cannot increase indefinitely. The surface tension force responsible for maintaining discrete droplet volumes can become overshadowed by the inertial forces at the time of collision. The nondimensional number that scales this force imbalance is the Weber number:

$$We = \frac{\rho U_{rel}^2 L_{ch}}{\sigma_{ST}} \tag{20}$$

In the relation, ρ and σ_{ST} are the fluid density and surface tension, respectively. For unconfined droplet collisions, a We number greater than 20 results in droplet breakup [30]. There is to date no experimental study that examines inertial droplet breakup in a confined microchannel. For liquid droplets in a gaseous microchannel flow, the droplets are in direct contact with portions of the channel walls. These confined interactions should suppress droplet breakup such that discrete droplet volumes are maintained for a We number larger than that predicted for unconfined flows. The We number ranged from 10^{-2} to 10^{-1} for the droplet length and velocity scales examined in this work.

For a fixed droplet length scale, this suggests that droplet relative velocity at the time of collision can be increased by a factor of three before the We number reaches unity. Assuming the ratio of mixing to convection time scales is maintained, the mixing time would be reduced by one-third.

CONCLUSIONS

This article describes an experimental investigation of droplet collisions and subsequent mixing in a confined microchannel. A high-speed gaseous flow is used to detach and transport discrete liquid droplets to a collision zone where the droplets collide, coalesce, and mix. The degree of mixing is determined by the statistics of the spatial intensity distribution of a conserved fluorescent tracer dye. The time required for mixing occurs when the intensity field is homogenous and the standard deviation reaches a minimum. Mixing times near 600 μs have been demonstrated using this technique for nanoliter droplet volumes.

Insight into the experimental mixing results is obtained by comparing the actual mixing time to the relevant system time scales for mass diffusion, momentum diffusion, and convection The analysis reveals that as droplet inertia is increased (Pe, $Re \gg 1$), the ratio of mixing to convection time obtained a constant value near 5 and suggests that mixing time follows the convective time scale under inertial conditions. In contrast, the ratio of mixing time to viscous and mass diffusion time was nearly constant in the low droplet Re number regime and began to decrease in opposition to droplet inertia.

The results show how the effective length scale for mass diffusion decreased with increasing droplet inertia. By taking the ratio of the effective mass diffusion length scale to the characteristic droplet length scale results in a $Pe^{-1/2}$ dependence as droplet inertia is increased. This result is extended to show that the ratio of effective to actual mass diffusivity was directly proportional to Pe. Thus, the net result of inertial mixing is a decrease in the effective diffusion length scale or an increase in the apparent mass diffusivity. For the range of Pe numbers considered in the work, the apparent mass diffusivity increased by a factor of 10^5. Further tests are needed to verify if this trend persists beyond the Re and Pe number range consider in this study. However, increasing droplet velocity prior to collision demands increased temporal resolution in order to capture the highly dynamic collision process.

These results also suggest that there is significant potential for increasing droplet mixing rates in a confined microchannel simply by increasing the droplet convective time scale prior to collision. The limiting factor may be the onset of droplet breakup, which occurs once the inertial force exceeds the surface tension force that maintains the discrete droplet volume. The fastest mixing time achieved during these experiments was approximately 600 μs for a We number of 0.3. Assuming droplet breakup occurs at a We number of unity and maintaining a constant length scale on the order of the channel hydraulic diameter, the relative collisional velocity can be increased by a factor of

three before the onset of breakup occurs. Since the mixing rate is proportional to collision velocity, the mixing time can be reduced by a factor of three. This is a conservative estimate since the presence of channel walls suppresses droplet breakup to a much higher degree than unconfined droplet collisions. The ability to verify this hypothesis in the laboratory is limited by the optical diagnostic hardware used to quantify mixing rates. As camera frame rate is increased, the received fluorophore emission signal and the ability to resolve temporal changes in the spatial intensity distribution decrease substantially.

Although not fully characterized, tracer visualization shows the presence complex vortical structures during the mixing process. Such structures play a major role mixing by quickly and effectively rearranging the coalesced droplet volume and providing more interfacial area for diffusion to act. It is not clear if the dominate origin of these structures is the collision event or the detachment entrainment process prior to the collision.

NOMENCLATURE

D	mass diffusivity, $m^2.s^{-1}$
D_{eff}	effective mass diffusivity, $m^2.s^{-1}$
I	intensity, dimensionless
L_{ch}	characteristic droplet length scale, m
N	number of image pixels, dimensionless
N_f	number of image frames, dimensionless
Pe	Peclet number, dimensionless
Re	Reynolds number, dimensionless
Re_{Dh}	Reynolds number based on channel hydraulic diameter, dimensionless
Sc	Schmidt number, dimensionless
t_{Mix}	actual mixing time, s
U_{rel}	relative droplet velocity, $m.s^{-1}$
Vol	droplet volume, m^3
We	Weber number, dimensionless

Greek Symbols

α	positive number, dimensionless
β	positive number, dimensionless
μ	average intensity, dimensionless
μ_f	average intensity of an image frame, dimensionless
ν	fluid viscosity, $m^2.s^{-1}$
ρ	density, $kg.m^{-3}$
σ	standard deviation of intensity, dimensionless
σ_f	image frame standard deviation of intensity, dimensionless
σ_{ST}	surface tension, $J.m^{-2}$
τ_{Conv}	convective time constant, s
τ_{Diff}	mass diffusion time constant, s
τ_{Visc}	viscous time constant, s

REFERENCES

[1] Breakthrough of the Year—The Runners-Up: Molecular Dynamic Simulations, *Science*, vol. 330, no. 6011, pp. 1605–1607, 2010.

[2] Liu, R. H., Yang, J., Pindera, M. Z., Athavale, M., and Grodzinski, P., Bubble-Induced Acoustic Micromixing, *Lab on a Chip*, vol. 2, no. 3, pp. 151–157, 2002.

[3] O'Driscoll, C., Music-Driven Lab-on-a-Chip Hits the Right Notes, *Chemistry and Industry*, no. 15, pp. 8, August, 2009.

[4] Ahmed, D., Mao, X., Shi, J., Juluri, B. K., and Huang, T. J., A Millisecond Micromixer via Single-Bubble-Based Acoustic Streaming, *Lab on a Chip*, vol. 9, no. 18, pp. 2738–2741, 2009.

[5] Yi-Kuen, L., Deval, J., Tabeling, P., and Chih-Ming, H., Chaotic Mixing in Electrokinetically and Pressure Driven Microflows, *IEEE International Conference on Microelectromechanical Systems*, Interlaken, Switzerland, pp. 483–486, 2001

[6] Oddy, M. H., Santiago, J. G., and Mikkelsen, J. C., Electrokinetic Instability Micromixing, *Analytical Chemistry*, vol. 73, no. 24, pp. 5822–5832, 2001.

[7] Chang, C., and Yang, R., Electrokinetic Mixing in Microfluidic Systems, *Microfluid Nanofluid*, vol. 3, no. pp. 501–525, 2007.

[8] Bau, H., Zhong, J., and Yi, M., A Minute Magnetohydrodynamic (MHD) Mixer, *Sensors and Actuators B*, vol. 79, no. pp. 205–213, 2001.

[9] Hellman, A. N., Rau, K. R., Yoon, H. H., Bae, S., Palmer, J. F., Phillips, K. S., Allbritton, N. L., and Venugopalan, V., Laser-Induced Mixing in Microfluidic Channels, *Analytical Chemistry*, vol. 79, no. 12, pp. 4484–4492, 2007.

[10] Delville, J., Vincent, M. d. S., Schroll, R., Chraibi, H., Issenmann, B., Wunenburger, R., Lasseux, D., Zhang, W., and Brasselet, E., Laser Microfluidics: Fluid Actuation by Light, *Journal of Optics A: Pure and Applied Optics*, vol. 11, no. p. 034015, 2009.

[11] Cola, B., Schaffer, D., Fisher, T., and Stremler, M., A Pulsed Source-Sink Fluid Mixing Device, *Journal of Microelectromechanical Systems*, vol. 15, no. 1, pp. 259–266, 2006.

[12] Takahashi, S., Ching, Y., Wang, J., and Rouseau, D. L., Microsecond Generation of Oxygen-Bound Cytochrome *c* Oxidase by Rapid Solution Mixing, *Journal of Biological Chemistry*, vol. 270, no. 15, pp. 8405–8407, 1995.

[13] Zhang, Z., Zhao, P., and Xiao, G., Focused-Enhanced Mixing in Microfluidic Channels, *Biomicrofluidics*, vol. 2, pp. 014101–014109, 2008.

[14] Knight, J. B., Vishwanath, A., Brody, J. P., and Austin, R. H., Hydrodynamic Focusing on a Silicon Chip: Mixing Nanoliters in Microseconds, *Physical Review Letters*, vol. 80, no. 17, pp. 3863–3866, 1998.

[15] Hertzog, D. E., Michalet, X., Jager, M., Kong, X., Santiago, J. G., Weiss, S., and Bakajin, O., Femtomole Mixer for Microsecond Kinetic Studies of Protein Folding, *Analytical Chemistry*, vol. 76, no. 24, pp. 7169–7178, 2004.

[16] Aref, H., Stirring by Chaotic Advection, *Journal of Fluid Mechanics*, vol. 143, pp. 1–21, 1984.

[17] Stroock, A. D., Dertinger, S. K., Ajdari, A., Mezic, I., Stone, H. A., and Whitesides, G. M., Chaotic Mixer for Microchannels, *Science*, vol. 295, no. 5555, pp. 647–651, 2002.

[18] Mao, X., Juluri, B., Lapsley, M., Stratton, Z., and Huang, T., Milliseconds Microfluidic Chaotic Bubble Mixer, *Microfluidics and Nanofluidics*, vol. 8, no. 1, pp. 139–144, 2010.

[19] Tice, J. D., Song, H., et al., Formation of Droplets and Mixing in Multiphase Microfluidics at Low Values of the Reynolds and the Capillary Numbers, *Langmuir*, vol. 19, pp. 9127–9133, 2003.

[20] Song, H., Bringer, M. R., Tice, J. D., Gerdts, C. J., and Ismagilov, R. F., Experimental Test of Scaling of Mixing by Chaotic Advection in Droplets Moving Through Microfluidic Channels, *Applied Physics Letters*, vol. 83, no. 12, pp. 4664–4666, 2003.

[21] Song, H., Chen, D. L., and Ismagilov, R. F., Reactions in Droplets in Microfluidic Channels, *Angewandte Chemie Int. Ed. English*, vol. 45, no. 44, pp. 7336–7356, 2006.

[22] Song, H., and Ismagilov, R. F., Millisecond Kinetics on a Microfluidic Chip Using Nanoliters of Reagents, *Journal of the American Chemical Society*, vol. 125, no. 47, pp. 14613–14619, 2003.

[23] Wang, J., Feng, L., Ottino, J. M., and Lueptow, R., Inertial Effects on Chaotic Advection and Mixing in a 2D Cavity Flow, *Industrial & Engineering Chemistry Research*, vol. 48, no. 5, pp. 2436–2442, 2008.

[24] Xia, H., Wan, S., Shu, C., and Chew, Y., Chaotic Micromixers Using Two-Layer Crossing Channels to Exhibit Fast Mixing at Low Reynolds Numbers, *Lab on a Chip*, vol. 5, pp. 748–755, 2005.

[25] Simonnet, C., and Groisman, A., Chaotic Mixing in a Steady Flow in a Microchannel, *Physical Review Letters*, vol. 94, pp. 134501, 2005.

[26] Carroll, B., and Hidrovo, C., An Experimental Investigation of Droplet Detachment in High-Speed Microchannel Air Flow, *2nd ASME Micro/Nanoscale Heat & Mass Transfer International Conference (MNHMT09)*, Shanghai, China, vol. 18491, pp. 1–10, 2009.

[27] van der Graaf, S., Nisisako, T., Schroen, R., van der Sman, C., and Boom, R., Lattice Boltzmann Simulations of Droplet Formation in a T-Shaped Microchannel, *Langmuir*, vol. 22, pp. 4144–4152, 2006.

[28] Dimotakis, P. E., Turbulent Mixing, *Annual Review of Fluid Mechanics*, vol. 37, no. 1, pp. 329–356, 2005.

[29] Arbeloa, F. L., Arbeloa, T. L., Arbeloa, I. L., Moreno, I. G., Costela, A., Sastre, R., and Amat-Guerri, F., Photophysical and Lasing Properties of Pyrromethene 567 Dye in Liquid Solution, *Chemical Physics*, vol. 236, pp. 331–341, 1998.

[30] Qian, J., and Law, C. K., Regimes of Coalescence and Separation in Droplet Collision, *Journal of Fluid Mechanics*, vol. 331, no. 1, pp. 59–80, 1997.

Brian Carroll is a Ph.D. student at the University of Texas at Austin and graduate researcher in the Multiscale Thermal Fluid Laboratory. He received his M.S. in mechanical engineering at the University of Texas at Austin in 2004 and worked as a thermal engineer at the Jet Propulsion Laboratory before beginning his Ph.D. studies. His research focuses on droplet dynamics in confined microchannel flow with an emphasis on droplet generation, transport, and mixing in a high-speed gaseous continuous phase. Much of this effort is directed toward developing an optical diagnostic technique using differential fluorescent measurements that provides quantitative mixing information in highly dynamic droplet mixing events.

Carlos Hidrovo is an assistant professor of mechanical engineering at the University of Texas at Austin. He earned his Ph.D. in mechanical engineering from the Massachusetts Institute of Technology in 2001. He worked as a research scientist in the 3D Optical Systems group at MIT and as a research associate in the Micro Heat Transfer Laboratory at Stanford University before joining the faculty of the University of Texas at Austin in September 2007. He is the recipient of the American Society of Mechanical Engineering 2001 Robert T. Knapp Award and the 2008 DARPA Young Faculty Award. His research interests lie at the intersection of multiscale and multiphase flow and transport phenomena, surface tension interactions in micro-/nanoengineered structures, and electrokinetic ion transport in porous media for applications in energy, portable biochemical diagnostics, thermal management, and water treatment systems. He is also actively involved in developing novel imaging and diagnostic tools in these areas.